nanomaterials

MDPI

Article

Two-Dimensional Core-Shell Structure of Cobalt-Doped@MnO_2 Nanosheets Grown on Nickel Foam as a Binder-Free Battery-Type Electrode for Supercapacitor Application

Md Moniruzzaman [1], Yedluri Anil Kumar [2,3], Mohan Reddy Pallavolu [4], Hammad Mueen Arbi [2,3], Salem Alzahmi [3,5,*] and Ihab M. Obaidat [2,3,*]

[1] Department of Chemical and Biological Engineering, Gachon University, 1342 Seongnam-daero, Seongnam-si 13120, Gyeonggi-do, Korea
[2] Department of Physics, United Arab Emirates University, Al Ain 15551, United Arab Emirates
[3] National Water and Energy Center, United Arab Emirates University, Al Ain 15551, United Arab Emirates
[4] School of Chemical Engineering, Yeungnam University, Gyeongsan 38541, Korea
[5] Department of Chemical & Petroleum Engineering, United Arab Emirates University, Al Ain 15551, United Arab Emirates
* Correspondence: s.alzahmi@uaeu.ac.ae (S.A.); iobaidat@uaeu.ac.ae (I.M.O.)

Abstract: Herein, we present an interfacial engineering strategy to construct an efficient hydrothermal approach by in situ growing cobalt-doped@MnO_2 nanocomposite on highly conductive nickel foam (Ni foam) for supercapacitors (SCs). The remarkably high specific surface area of Co dopant provides a larger contacting area for MnO_2. In the meantime, the excellent retentions of the hierarchical phase-based pore architecture of the cobalt-doped surface could beneficially condense the electron transportation pathways. In addition, the nickel foam (Ni foam) nanosheets provide charge-transport channels that lead to the outstanding improved electrochemical activities of cobalt-doped@MnO_2. The unique cobalt-doped@MnO_2 nanocomposite electrode facilitates stable electrochemical architecture, multi-active electrochemical sites, and rapid electro-transports channels; which act as a key factor in enhancing the specific capacitances, stability, and rate capacities. As a result, the cobalt-doped@MnO_2 nanocomposite electrode delivered superior electrochemical activities with a specific capacitance of 337.8 F g^{-1} at 0.5 A g^{-1}; this is greater than pristine MnO_2 (277.9 F g^{-1}). The results demonstrate a worthy approach for the designing of high-performance SCs by the grouping of the nanostructured dopant material and metal oxides.

Keywords: cobalt-doped manganese oxides; electrode; supercapacitors; energy storage; hydrothermal method

Citation: Moniruzzaman, M.; Anil Kumar, Y.; Pallavolu, M.R.; Arbi, H.M.; Alzahmi, S.; Obaidat, I.M. Two-Dimensional Core-Shell Structure of Cobalt-Doped@MnO_2 Nanosheets Grown on Nickel Foam as a Binder-Free Battery-Type Electrode for Supercapacitor Application. *Nanomaterials* **2022**, *12*, 3187. https://doi.org/10.3390/nano12183187

Academic Editors: Jeng-Yu Lin, Min-Hsin Yeh and Tzu-Ho Wu

Received: 25 August 2022
Accepted: 9 September 2022
Published: 14 September 2022

1. Introduction

The intemperate exploitations of fossil fuels have led us to energy consumption limits and unsustainable environmental difficulties [1–3]. Supercapacitors (SCs) are a new type of greener energy storing devices among batteries and capacitors that have the benefits of higher efficiency, larger power density, environmental protections, longer cycles, etc. [4–6]. However, the low energy densities of SCs limit their large-scale configuration commercially. An efficient route to enhance this energy density is to make asymmetric SCs [7–9].

Electrodes are one of the crucial elements influencing the performances of SCs [10]. Different types of material samples have been developed so far for achieving better energy densities, such as doped materials [11–13], metal hydroxides/oxides [14,15], composite electrodes [16–19], and conductive polymers [20–23]. From this perspective, MnO_2 becomes a favored source for making pseudocapacitor (PCs) electrodes due to their superior theoretical capacities (~1370 F g^{-1}), cheaper prices, and eco-friendliness [24]. MnO_2 would

deliver excellent capacities and characteristic features in neutral electrolytes, which do not need stronger acids or alkalic-type environments; in turn, this is good for the environment [25]. However, the MnO_2 conductivity is still poor; this issue can be solved by combining MnO_2 with a dopant material, which enables larger specific surface areas and excellent conductivities [26,27].

Cobalt-doped electrodes have features such as excellent electrical conductivities, good chemical stabilities, superior surface interfaces, and a cheaper price. Thus, it could be contemplated as an absolute candidate for supporting MnO_2 in forming a composite electrode sample [28]. The fabrication of cobalt-doped materials on nickel foam skeleton has attracted a lot of interest so far [4,29–31]. Nickel foam is safer, greener, and plentiful; thus, it became favorable for renewable energy developments. Cobalt-doped material on the nickel foam skeleton generally consists of superior surface area and porosities, which would efficaciously shorten the ion/electron transportation intervals. Nickel foam with cobalt-doped material handled with alkali or acids also has a plentiful functional surfacing group, which are favored for electrochemical activities [32–35]. Thus, the use of cobalt-doped material with nickel foam and MnO_2 has been anticipated to enhance the performances of both MnO_2 and cobalt-doped materials.

Herein, we developed a unique cobalt-doped MnO_2 with the conductive skeleton of nickel foam via a hydrothermal technique. The composite of cobalt-doped@MnO_2 delivers excellent energy storing performance. This would be ascribed to the excellent retention of the conductive way and uniformly loaded MnO_2. Cobalt-doped@MnO_2 facilitated the self-assembly of the composites with nickel foam; meanwhile, the metal oxides constructively enhanced the capacities by transmitting the composite with PCs. The energy storage performances of the cobalt-doped@MnO_2 nanosheets were synergistically developed, providing multiple chemical states of Co-existences in the electrode. The results manifested the specific capacitance of the cobalt-doped@MnO_2 nanosheets is 337.8 F g^{-1}at 0.5 A g^{-1}; this surpasses composites in recently reported literature.

2. Experimental Procedure

2.1. Synthesis of Cobalt-Doped@MnO_2 Composite Nanosheets

Before synthesis, nickel foam (2 × 1 cm^2) was carefully cleaned with a 6.0 M HCl solution in an ultrasound bath for 30 min to remove and eliminate the influence of the NiO layer from the surface; it was then rinsed with deionized water and absolute ethanol several times; and finally, dried in a vacuum oven at 50 °C. Cobalt nitrate hexahydrate (3 g) was added to 65 mL of $MnCl_2$ solution with a concentration of 0.034 mol L^{-1}. Then, the precursor solution was continuously treated with ultrasound for 20 min to permit the complete adsorption of Mn^{2+} on cobalt nitrate hexahydrate. In due course, the supernatant liquids were detached by centrifugation; and 65 mL of $KMnO_4$ solutions (0.069 M) were added to the mixtures. After stirring at 115 °C for 3 h, the precursor mixtures were washed with DI water continuously; and finally, dried at 130 °C for 12 h to gain the cobalt-doped@MnO_2 nanosheets composite.

For comparison, pure MnO_2 electrodes were also fabricated by a similar reaction process without adding Cobalt nitrate hexahydrate into the $MnCl_2$ solution.

2.2. Characterizations

The electrode morphology was investigated by scanning electron microscopy (FE-SEM, S-4800, Hitachi, Busan, Korea) and transmission electron microscopy (HRTEM, CJ111). The elemental compositions and chemical states of the spectroscopic procedures of the electrode were studied by X-ray photoelectron spectroscopy (XPS, VG Scientific—ESCALAB 250, Busan, Korea.). The electrode sample structure of the crystal was perceived by X-ray diffraction (XRD, D/Max-2400, Rigaku, Tokyo, Japan, Cu Kα) at an acceleration voltage of 40 kV using Cu Ka (λ = 0.154 nm) radiation.

2.3. Electrochemical Measurement

The electrochemical activities of the electrode composites (MnO_2 and cobalt-doped@MnO_2) were investigated by a three-electrode configuration operating an electrochemical workstation (SP-150 Biologic instrument, Busan, South Korea) in a 2 M KOH electrolyte. The Pt wire (2 cm × 2 cm) and Hg/HgO electrode were employed as the counter and reference electrodes, respectively. The galvanostatic charge/discharge (GCD), cyclic voltammetry (CV) tests quantifications, and electrochemical impedance spectroscopy (EIS) analysis were captured with a counter and reference electrode. The EIS result was processed by operating AC potentials of 10 mV amplitude (versus Hg/HgO) in the ranges of 200 mHz to 200 kHz frequencies at open-circuit potential (OCP). For a three-electrode system, the AC potential of 10 mV was applied versus RE. The mass loading of the working sample on each electrode is ~3.4 mg. The specific capacitance (C_s, F g^{-1}) was calculated from the charge–discharge curve by using the following equation [34]:

$$C_s = (I \times \Delta t)/(m \times \Delta V) \quad (1)$$

where C_s, I, Δt, and m are the specific capacitance (F g^{-1}), current (A), discharge time (s), and mass (g) of the active materials, respectively.

3. Results and Discussion

Figure 1 is a brief illustration of the preparation procedures for the cobalt-doped MnO_2 nanosheets composite. During the following hydrothermal procedures, the cobalt gradually transformed into a porous nickel foam structure. The cobalt dope supports the enhancement of the pore structures and provides the cobalt doping of the nickel form [29]. After a post in-situ hydrothermal deposition procedure, densely MnO_2 nanoparticles were grown on the nickel foam. The chemical reactions involved in the procedure are as follows:

$$2MnO_4^- + 3Mn^{2+} + 2H_2O \rightarrow 5MnO_2 + 4H^+ \quad (2)$$

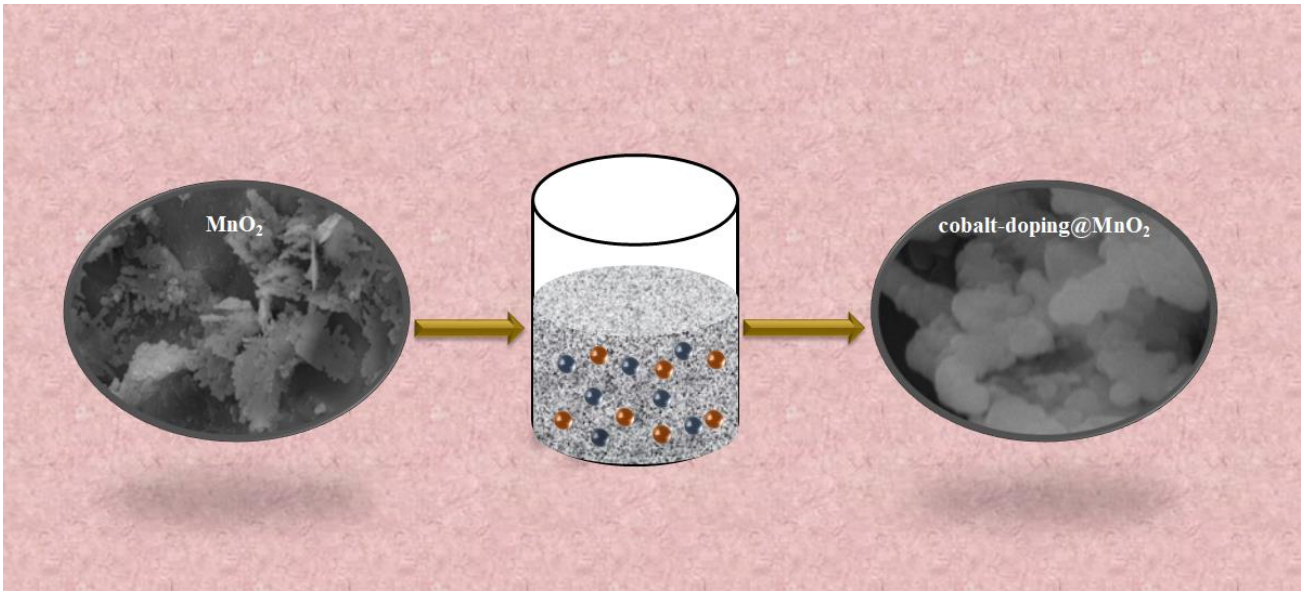

Figure 1. Schematic diagram of the cobalt-doped@MnO_2 nanosheets composite.

Figure 2a indicates a typical SEM image of the MnO_2 nanoparticle material. The MnO_2 nanoparticle appears with distinct porous architecture. The internally networked porous construction not only supplies a channel for quick electron transportations, but also acts as a well-being skeleton for the MnO_2 loading. Afterward, the SEM images of the cobalt-doped@MnO_2 nanosheets composite (Figure 2b) exhibits excellent dispersed MnO_2 nanoparticles uniformly coating on the interfaces of the nickel foam. Figure S1 shows the

SEM image of cobalt-doped@MnO_2 nanosheets composite well-distributed on the nickel foam. It is visible that the porous nature of the nickel foam is well-retained; this not only encourages the electrolyte ion transportations, but also produces a superior contacting surface for the MnO_2. The SEM structure analysis investigation obviously indicates that the cobalt-doped@MnO_2 nanosheets structure was facilitated by the excellent electron transportations between the electrode surface area and electrolyte interface to enhance the electrochemical performance. The different crystalline faces with polycrystalline characterization exist; and there was an observable grain boundary among the MnO_2 and cobalt dope in the structure of the cobalt-doped@MnO_2. TEM images (Figure 1) display the surface of the cobalt-doped@MnO_2 nanosheets composite, obviously disposing of dense nanoparticles loaded on the interfaces of the nickel foam. In addition, the HRTEM images (Figure 2d) of the MnO_2 nanoparticles disclose spacing fringes of 0.25 nm; this correlates to the (006) MnO_2 spacing planner. Further, the cobalt dope consists of numerous MnO_2 that connect to form a highly porous network structure; which helps the electrolyte ions penetrate during the charge–discharge process.

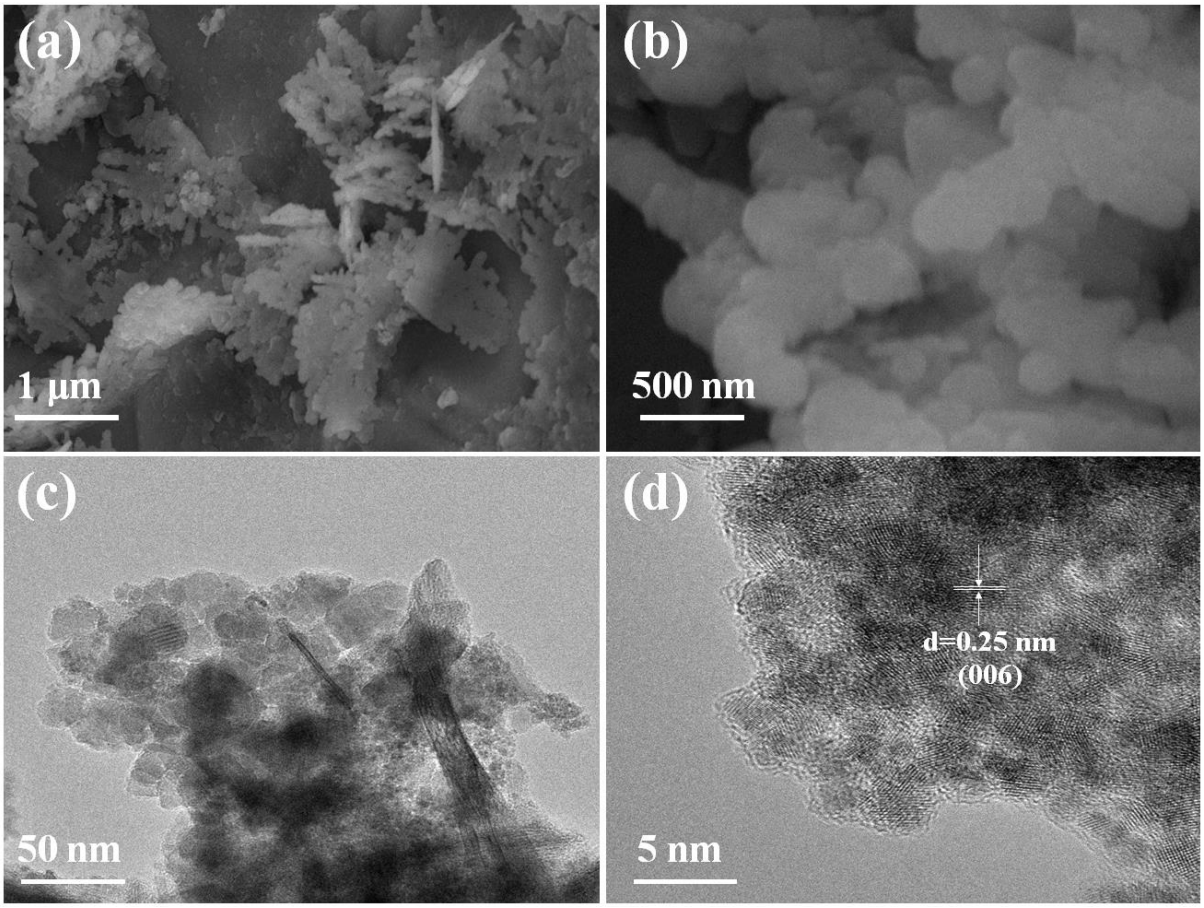

Figure 2. (**a**) SEM images of the MnO_2 sample; (**b**) an SEM image of the cobalt-doped@MnO_2 nanosheets composite; (**c**) a TEM image of the cobalt-doped@MnO_2 nanosheets composite; and (**d**) an HRTEM image revealing the crystalline structure of the MnO_2 nanosheets.

The crystalline structures of MnO_2 and the cobalt-doped@MnO_2 nanosheets composite were analyzed by XRD analysis, as depicted in Figure 3a. For the binary MnO_2 material, two sharp peaks are visible around 22° and 43.5°; these are similar to that of the nickel foam [34,35]. For the cobalt-doped@MnO_2 nanosheets composite, the three broader peaks at 12.3°, 36.8°, and 65.8° are correlated with (002), (006), and (119) planners of the birnessite category-MnO_2 (JCPDS 18-802), respectively [36,37]. It is known that binary MnO_2 is similar to MnO_2 in the composite through comparisons.

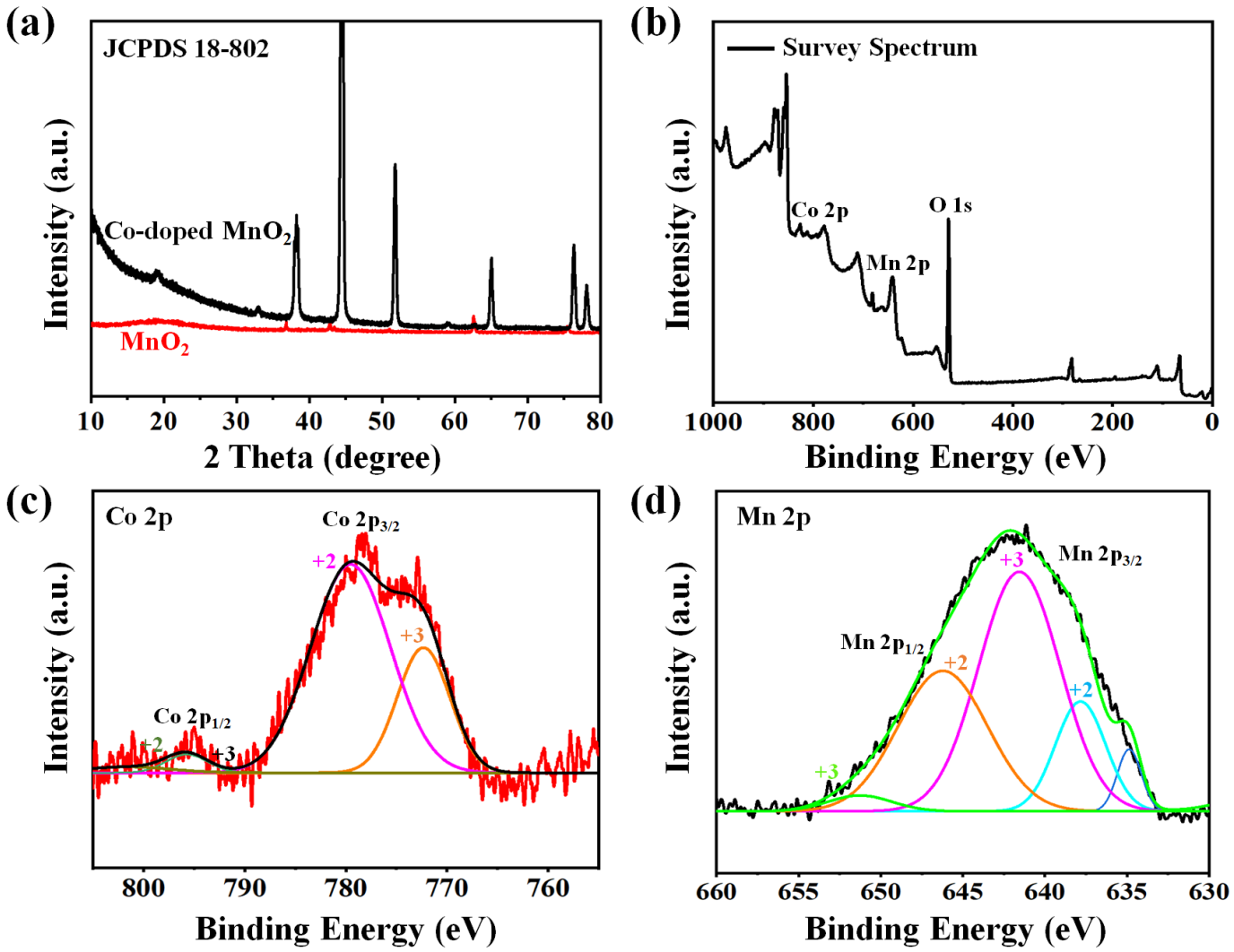

Figure 3. The XRD patterns (**a**) and wide-scan XPS spectra (**b**) of the cobalt-doped@MnO_2 nanosheets composite, respectively. (**c**,**d**) The high-resolution XPS spectra for the cobalt-doped@MnO_2 nanosheets composite of Co 2p and Mn 2p.

XPS investigations were further employed to obtain information on elemental structure compositions, and the chemical molecular states of the surfaces of the electrode. Figure 3b is the general mapping of the XPS spectrum. The cobalt-doped@MnO_2 nanosheets composite depicts the peaks of Co 2p, Mn 2p, C, and O elements. Furthermore, due to the loading of MnO_2, the Mn peaks are visible in the spectra of the cobalt-doped@MnO_2 nanosheets composite; and the C peaks decrease sharply. For the Co 2p XPS spectrum (Figure 3c), the spin-orbit split results of Co $2p_{1/2}$ (centered at 795 eV) and Co $2p_{3/2}$ (centered at 781 eV), transgression 15 eV; this reveals the coexistences of Co^{3+} and Co^{2+} cations [38,39]. By a Gaussian fitting method, the Co spectrum was fitted to four peaks, including the Co^{3+} peaks located at 780.8 eV and 781.1 eV and another peak located at 785.1eV and 802.5 eV, which was assigned to Co^{2+}. For the Mn 2p pattern (Figure 3d), the two peaks at 643.5 eV and 655.6 eV correspond to Mn $2p_{3/2}$ and Mn $2p_{1/2}$, respectively [40–42]. The fitting peak at 637.7 eV is particularly characteristic of Mn^{2+}, and the peaks located at 642.9 eV and 653.6 eV ascribed to Mn^{3+}. The spin separations energies were 11.9 eV, which reveals that the Mn valence states were +4 [34,43,44]. The O 1s spectra would be deconvoluted into O-C (531.5 eV), C-O-C/C-OH (533.4 eV), and O–Mn (530.2 eV) bondings, respectively (as showed in Figure S2). The presence of the cobalt dope group was favored for the enhancement of electrochemical capabilities [32].

Electrochemical Properties of Electrode Materials

The electrochemical capabilities of binary MnO_2 nanoparticles and the cobalt-doped@MnO_2 nanosheets composite were investigated using a three-electrode setup. The CV and GCD data values of the cobalt-doped@MnO_2 nanosheets composite were depicted in Figure 4a,b, respectively. As the scan rates expand between 5 to 200 mV s^{-1}, the CV plots remain in almost rectangular shapes; manifesting that the sample material consists of excellent reversibility and absolute capacitance nature. There were not any apparent redox peaks under the voltage windows of 0.0–0.6 V; which illustrates the behavior of the PCs of MnO_2 and the PC nature of the cobalt-doped@MnO_2 nanosheets composite. At various current densities between 0.5 A g^{-1} to 15 A g^{-1}, the GCD pattern shows close symmetrical charge/discharges (Figure 4b). At a 0.5 A g^{-1} current density, we performed the comparison of both binary MnO_2 nanoparticles and cobalt-doped@MnO_2 nanosheets composite electrodes (Figure 4c). We also investigated the CV curve of binary MnO_2 electrodes, as illustrated in Figure S3b. The CV curves comparison (Figure S3a) of the binary MnO_2 nanoparticles and cobalt-doped@MnO_2 nanosheets composite also display rectangular-type shapes. It is visible from the regions of the CV plots that the specific capacitances of the cobalt-doped@MnO_2 nanosheets composite are greater than that of binary MnO_2.

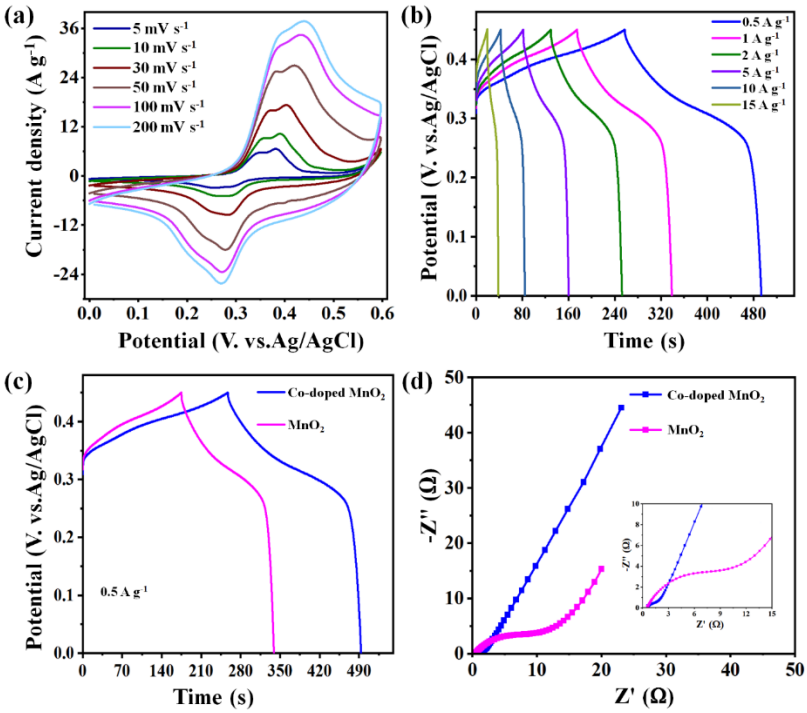

Figure 4. Electrochemical performances with the three-electrode system. (**a**) CV and (**b**) GCD curves of the cobalt-doped@MnO_2 nanosheets composite. (**c**) GCD curves at a current density of 0.5 A g^{-1} of binary MnO_2 nanoparticles and cobalt-doped@MnO_2 nanosheets composite electrode materials. (**d**) The Nyquist plots of binary MnO_2 and cobalt-doped@MnO_2 nanosheets composite electrode materials.

The data of EIS (Figure 4d) further evidenced that the cobalt-doped@MnO_2 nanosheets composite consists of good electrochemical performances. The range in the frequencies of the pattern was from 0.02 Hz to 200 KHz. The Nyquist diagrams of binary MnO_2 nanoparticles and cobalt-doped@MnO_2 nanosheets composite electrode materials achieve the same small semicircles in the higher-frequency ranges (the semicircle diameter reveals charge transfer resistances (R_{ct})); manifesting that they have smaller charge transfer resistances. The R_{ct} of the cobalt-doped@MnO_2 nanosheets composite was slightly greater than that of binary MnO_2 nanoparticles. This was due to the charge transfer of cobalt-doped@MnO_2 nanosheets presuming redox reactions, which were more moderate than the surface des-

orption/adsorption nature of the sample PCs [38]. In addition, it would be obvious that the cobalt-doped@MnO_2 nanosheets composite effectively enhances the conductivities of binary MnO_2 nanoparticles. The ideal capacitance character is apparent from the almost vertical linear plots in the lower frequency area. Thus, the cobalt-doped@MnO_2 nanosheets sample reveals a much more oblique plot; this signifies the foremost performances of the PCs.

Figure 5a displays the comparison of binary MnO_2 nanoparticles and cobalt-doped@MnO_2 nanosheets composite GCD plots at 0.5 A g^{-1}, respectively. The specific capacitance of binary MnO_2 nanoparticles was calculated to be 277.9 F g^{-1}, which is approximately only 1/3 of the cobalt-doped@MnO_2 nanosheets composite. These results illustrate that the porous behavior of the cobalt-doped@MnO_2 nanosheets composite is advantageous to the electrolyte ions of diffusion. While conserving binary MnO_2 nanoparticles' PC capacitance, the cobalt-doped@MnO_2 nanosheets composite electrode also expands PC capacitances.

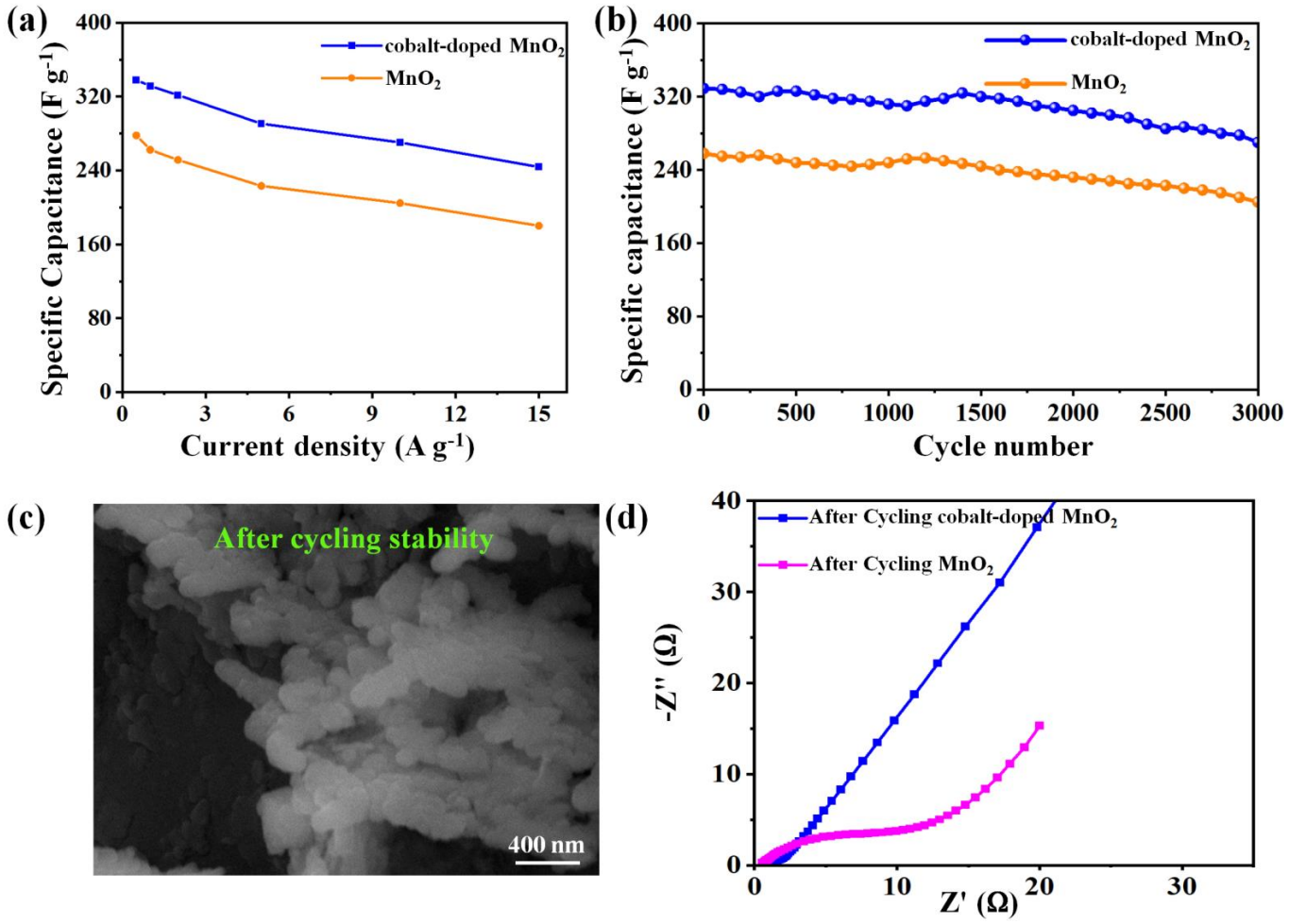

Figure 5. (**a**) Specific capacitances of binary MnO_2 nanoparticles and cobalt-doped@MnO_2 nanosheets composite electrodes; (**b**) charge–discharge cycling stability of binary MnO_2 nanoparticles and cobalt-doped@MnO_2 nanosheets composite electrodes at 2 A g^{-1}; (**c**) an SEM image of after 3000 long cycles; and (**d**) an Nyquist plot of after 3000 GCD cycles of binary MnO_2 nanoparticles and cobalt-doped@MnO_2 nanosheets composite electrodes.

According to the cycling test (Figure 5b), binary MnO_2 nanoparticles consist of well-cycled stabilities; and the capacity retention rate residues ~76.4% after 3000 long cycles. Whereas, for the cobalt-doped@MnO_2 nanosheets composite, the electrode remains ~82.5% after 3000 long cycles; manifesting that the nickel foam effectively enhances the cycling capabilities of MnO_2. Surprisingly, both binary MnO_2 nanoparticles and cobalt-doped@MnO_2

nanosheets composite electrodes have excellent retention stabilities. The specific capacitance performances of the MnO_2-based composite samples reported in previous studies are displayed in Table 1. The specific capacitances of the cobalt-doped@MnO_2 nanosheets composite electrode are much higher than that of some nickel foam-based MnO_2 composite materials and other MnO_2-based composites. Figure 5c illustrates the SEM image of the cobalt-doped@MnO_2 nanosheets composite material after 3000-long cycling stability. The SEM image shows a good surface structure and super-wettability, indicating a vital role in keeping faradaic redox and energy storage reactions. Figure 5d shows the impedance plots of the binary MnO_2 nanoparticles and cobalt-doped@MnO_2 nanosheets composite electrodes after 3000 cycles. There were no obvious changes of R_{ct} after 3000 long cycles, manifesting a rapid electron/ion transfer. Surprisingly, the higher performances of the cobalt-doped@MnO_2 nanosheets composite with hierarchical structure on nickel foam is beneficial; owing to the larger surface area accessing point for ions that enhance the wettability of the composite and accelerate electron transfer.

Table 1. MnO_2 composite electrode performance comparison over the last five years.

Electrode	Electrolyte	Specific Capacitance ($F\ g^{-1}$)	Current Density ($A\ g^{-1}$)	Ref.
MnO_2/rice husk-derived composite	0.5 M Na_2SO_4	210.3	0.5	[30]
Holey reduced graphene oxide/MnO_2 composites	1 M Na_2SO_4	192.2	0.5	[37]
MnO_2@CCNs	1 M Na_2SO_4	262	0.2	[38]
CNT@NCT@MnO_2	1 M Na_2SO_4	210	0.5	[40]
δ-$MnO_{2(4.0)}$/HRGO	1 M Na_2SO_4	245	1	[45]
α-MnO_2 NWs@δ-MnO_2 NSs	6 M KOH	310.2	0.5	[46]
PPy/mesoporous MnO_2	1 M Na_2SO_4	320	0.5	[47]
D-MNS-A@MnO_2	1 M Na_2SO_4	231	1	[48]
cobalt-doped@MnO_2 nanosheets	2 M KOH	337.8	0.5	This Work

4. Conclusions

In summary, cobalt-doped nanoparticles were uniformly grown on MnO_2 with a large specific surface region and unique pore construction to form a cobalt-doped@MnO_2 nanosheets composite. The improved electrochemical performances of the cobalt-doped@MnO_2 nanosheets composite are ascribed to the higher electrical conductivities, enlarged surface region, ample working electrochemical sites, and rapid charging-transfer channels. The cobalt-doped@MnO_2 nanosheets composite achieved extraordinary electrochemical capabilities. At a current density of 0.5 A g^{-1}, the specific capacitance is 337.8 F g^{-1}. Moreover, the cobalt-doped@MnO_2 nanosheets composite electrodes exhibit excellent cycling stabilities of 82.5% capacity retention at 3000 GCD long cycles. The results of this research support the use of metal oxides as conductive bases and expand the scope of dopant-based material applications. Finally, the cobalt-doped@MnO_2 nanosheets with the above unique physicochemical characteristics can have numerous good functionalities for other applications, such as biosensors, electrocatalysts, and batteries.

Supplementary Materials: The following supporting information can be downloaded at: https://www.mdpi.com/article/10.3390/nano12183187/s1, 1. Materials and Reagents; Figure S1. SEM image of cobalt-doped@MnO_2 nanosheets well distributed on nickel foam; Figure S2. XPS spectra of O 1s; Figure S3a. CV comparison of binary MnO_2 nanoparticles and cobalt-doped@MnO_2 nanosheets composite; Figure S3b. CV curves of binary MnO_2 nanoparticles. All authors have read and agreed to the published version of the manuscript.

Author Contributions: Conceptualization, I.M.O., Y.A.K., M.M. and S.A.; supervision and validation, I.M.O. and S.A.; investigation and writing, Y.A.K., M.M. and I.M.O.; investigation and visualization, M.R.P.; validation, H.M.A. All authors have read and agreed to the published version of the manuscript.

Funding: This research was funded by the UAEU-Strategic research program under grant no. 12R128.

Institutional Review Board Statement: Not applicable.

Informed Consent Statement: Not applicable.

Data Availability Statement: No new data were created or analyzed in this study. Data sharing is not applicable to this article.

Acknowledgments: This work was financially supported by the UAEU-Strategic research program under grant no. 12R128.

Conflicts of Interest: The authors declare no conflict of interest.

References

1. Yoon, J.H.; Kumar, Y.A.; Sambasivam, S.; Hira, S.A.; Krishna, T.N.V.; Zeb, K.; Uddin, W.; Kumar, K.D.; Obaidat, I.M.; Kim, S.; et al. Highly efficient copper-cobalt sulfide nano-reeds array with simplistic fabrication strategy for battery-type supercapacitors. *Energy Stor.* **2020**, *32*, 101988. [CrossRef]
2. Mun, C.H.; Gopi, C.V.V.M.; Vinodh, R.; Sambasivam, S.; Obaidat, I.M.; Kim, H.J. Microflower-like nickel sulfide-lead sulfide hierarchical composites as binder-free electrodes for high-performance supercapacitors. *J. Energy Stor.* **2019**, *26*, 100925. [CrossRef]
3. Kumar, Y.A.; Sambasivam, S.; Hira, S.A.; Zeb, K.; Uddin, W.; Krishna, T.N.V.; Kumar, K.D.; Obaidat, I.M.; Kim, H.J. Boosting the energy density of highly efficient flexible hybrid supercapacitors via selective integration of hierarchical nanostructured energy materials. *Electrochim. Acta* **2020**, *364*, 137318. [CrossRef]
4. Zheng, J.; Yan, B.; Feng, L.; Zhang, Q.; Zhang, C.; Yang, W.; Han, J.; Jiang, S.; He, S. Potassium citrate assisted synthesis of hierarchical porous carbon materials for high performance supercapacitors. *Diam. Relat. Mater.* **2022**, *128*, 109247. [CrossRef]
5. Zheng, S.; Zhang, J.; Deng, H.; Du, Y.; Shi, X.J. Chitin derived nitrogen-doped porous carbons with ultrahigh specific surface area and tailored hierarchical porosity for high performance supercapacitors. *Bioresour. Bioprod.* **2021**, *6*, 142–151. [CrossRef]
6. Gopi, C.V.V.M.; Vinodh, R.; Sambasivam, S.; Obaidat, I.M.; Kalla, R.M.N.; Kim, H.J. One-pot synthesis of copper oxide–cobalt oxide core–shell nanocactus-like heterostructures as binder-free electrode materials for high-rate hybrid supercapacitors. *Mater. Today Energy* **2019**, *14*, 100358. [CrossRef]
7. Chen, L.; Wang, F.; Tian, Z.; Guo, H.; Cai, C.; Wu, Q.; Du, H.; Liu, K.; Hao, Z.; He, S.; et al. Wood-Derived High-Mass-Loading MnO_2 Composite Carbon Electrode Enabling High Energy Density and High-Rate Supercapacitor. *Small* **2022**, *18*, 2201307. [CrossRef]
8. Kumar, Y.A.; Kim, H.-J. Preparation and electrochemical performance of $NiCo_2O_4$@$NiCo_2O_4$ composite nanoplates for high performance supercapacitor applications. *New J. Chem.* **2018**, *42*, 19971–19978. [CrossRef]
9. Niu, L.; Wu, T.; Chen, M.; Yang, L.; Yang, J.; Wang, Z.; Kornyshev, A.A.; Jiang, H.; Bi, S.; Feng, G. Conductive Metal-organic frameworks for supercapacitors. *Adv. Mater.* **2022**. [CrossRef]
10. Lee, Y.S.; Kumar, Y.K.; Sambasivam, S.; Hira, S.A.; Zeb, K.; Uddin, W.; Reddy, S.P.R.; Kumar, K.D.; Obaidat, I.M.; Kim, H.J.; et al. $CoCu_2O_4$ nanoflowers architecture as an electrode material for battery type supercapacitor with improved electrochemical performance. *Nano-Struct. Nano-Objects* **2020**, *24*, 100618. [CrossRef]
11. Xie, P.; Yuan, W.; Liu, X.; Peng, Y.; Yin, Y.; Li, Y.; Wu, Z. Advanced carbon nanomaterials for state-of-the-art flexible supercapacitors. *Energy Storage Mater.* **2021**, *36*, 56–76. [CrossRef]
12. Yedluri, A.K.; Kim, H.-J. Wearable super-high specific performance supercapacitors using a honeycomb with folded silk-like composite of NiCo2O4 nanoplates decorated with NiMoO4 honeycombs on nickel foam. *Dalton Trans.* **2018**, *47*, 15545–15554. [CrossRef] [PubMed]
13. Yedluri, A.K.; Anitha, T.; Kim, H.-J. Fabrication of Hierarchical NiMoO4/$NiMoO_4$ Nanoflowers on Highly Conductive Flexible Nickel Foam Substrate as a Capacitive Electrode Material for Supercapacitors with Enhanced Electrochemical Performance. *Energies* **2019**, *12*, 1143. [CrossRef]
14. Sharma, P.; Sundaram, M.M.; Watcharatharapong, T.; Jungthawan, S.; Ahuja, R. Tuning the Nanoparticle Interfacial Properties and Stability of the Core–Shell Structure in Zn-Doped $NiMoO_4$@AWO_4. *ACS Appl. Mater. Interfaces* **2021**, *13*, *47*, 56116–56130. [CrossRef]
15. Wickramaarachchi, K.; Sundaram, M.M.; Henry, D.J.; Gao, X. Alginate Biopolymer Effect on the Electrodeposition of Manganese Dioxide on Electrodes for Supercapacitors. *ACS Appl. Energy Mater.* **2021**, *4*, 7040–7051. [CrossRef]
16. Wang, C.; Wang, J.; Wu, W.; Qian, J.; Song, S.; Yue, Z.J. Feasibility of activated carbon derived from anaerobic digester residues for supercapacitors. *Power Sources* **2019**, *412*, 683–688. [CrossRef]
17. Brousse, T.; Bélanger, D.; Long, J.W. To be or not to be pseudocapacitive? *J. Electrochem. Soc.* **2015**, *162*, A5185. [CrossRef]

18. Gu, C.; Ge, X.; Wang, X.; Tu, J.J. Cation–anion double hydrolysis derived layered single metal hydroxide superstructures for boosted supercapacitive energy storage. *Mater. Chem. A* **2015**, *3*, 14228–14238. [CrossRef]
19. Chhetri, K.; Tiwari, A.P.; Dahal, B.; Ojha, G.P.; Mukhiya, T.; Lee, M.; Kim, T.; Chae, S.; Muthurasu, A.; Kim, H.Y. A ZIF-8-derived nanoporous carbon nanocomposite wrapped with Co_3O_4-polyaniline as an efficient electrode material for an asymmetric supercapacitor. *J. Electroanal. Chem.* **2020**, *856*, 113670. [CrossRef]
20. Chhetri, K.; Dahal, B.; Mukhiya, T.; Tiwari, A.P.; Muthurasu, A.; Kim, H.Y. Integrated hybrid of graphitic carbon-encapsulated Cu_xO on multilayered mesoporous carbon from copper MOFs and polyaniline for asymmetric supercapacitor and oxygen reduction reactions. *Carbon* **2021**, *179*, 89–99. [CrossRef]
21. Yang, Y.; Wang, X.; Huang, F.; Zhao, J.; Wang, X. $Ni(OH)_2$ nanodot-decorated Co-Co LDH/C hollow nanocages for a high performance supercapacitor. *Dalton Trans.* **2020**, *49*, 17310–17320. [CrossRef] [PubMed]
22. Zhang, J.; Wang, Z.; Deng, T.; Zhang, W. $Ni(OH)_2$ derived Ni-MOF supported on carbon nanowalls for supercapacitors. *Nanotechnology* **2021**, *32*, 195404. [CrossRef] [PubMed]
23. Xin, Y.; Dai, X.; Lv, G.; Wei, X.; Li, S.; Li, Z.; Xue, T.; Shi, M.; Zou, K.; Chen, Y.; et al. Stability-Enhanced α-$Ni(OH)_2$ Pillared by Metaborate Anions for Pseudocapacitors. *ACS Appl. Mater. Interf.* **2021**, *13*, 28118–28128. [CrossRef]
24. Zhao, Y.F.; Ran, W.; He, J.; Huang, Y.Z.; Liu, Z.F.; Liu, W.; Tang, Y.F.; Zhang, L.; Gao, D.W.; Gao, F.M. High-performance asymmetric supercapacitors based on multilayer MnO_2/graphene oxide nanoflakes and hierarchical porous carbon with enhanced cycling stability. *Small* **2015**, *11*, 1310–1319. [CrossRef] [PubMed]
25. Zhang, S.W.; Yin, B.S.; Liu, X.X.; Gu, D.M.; Gong, H.; Wang, Z.B. A high energy density aqueous hybrid supercapacitor with widened potential window through multi approaches. *Nano Energy* **2019**, *59*, 41–49. [CrossRef]
26. Hu, L.B.; Chen, W.; Xie, X.; Liu, N.; Yang, Y.; Wu, H.; Yao, Y.; Pasta, M.; Alshareef, H.N.; Cui, Y. Symmetrical MnO_2-carbon nanotube-textile nanostructures for wearable pseudocapacitors with high mass loading. *ACS Nano* **2011**, *5*, 8904–8913. [CrossRef]
27. Cao, R.Y.; Yang, H.C.; Deng, X.L.; Sun, P.X.; Zhang, S.W.; Xu, X.J. Construction of 3DOM carbon nitrides with quasi-honeycomb structures for efficient photocatalytic H_2 production. *ChemCatChem* **2018**, *10*, 5656–5664. [CrossRef]
28. Li, H.X.; Ma, S.; Cai, H.Q.; Zhou, H.H.; Huang, Z.Y.; Hou, Z.H.; Wu, J.J.; Yang, W.J.; Yi, H.B.; Fu, C.P.; et al. Ultra-thin Fe_3C nanosheets promote the adsorption and conversion of polysulfides in lithium-sulfur batteries. *Energy Storage Mater.* **2019**, *18*, 338–348. [CrossRef]
29. Yuan, Y.; Jia, H.; Liu, Z.; Wang, L.; Sheng, J.; Fei, W. A highly conductive $Ni(OH)_2$ nano-sheet wrapped $CuCo_2S_4$ nano-tube electrode with a core-shell structure for high performance supercapacitors. *Dalton Trans.* **2021**, *50*, 8476–8486. [CrossRef]
30. Yuan, C.J.; Lin, H.B.; Lu, H.Y.; Xing, E.D.; Zhang, Y.S.; Xie, B.Y. Synthesis of hierarchically porous MnO_2/rice husks derived carbon composite as high-performance electrode material for supercapacitors. *Appl. Energy* **2016**, *178*, 260–268. [CrossRef]
31. Dong, B.; Li, M.; Chen, S.; Ding, D.; Wei, W.; Gao, G.; Ding, S. Formation of g-C_3N_4@$Ni(OH)_2$ Honeycomb Nanostructure and Asymmetric Supercapacitor with High Energy and Power Density. *ACS Appl. Mater. Interf.* **2017**, *9*, 17890–17896. [CrossRef] [PubMed]
32. Sun, W.; Rui, X.; Ulaganathan, M.; Madhavi, S.; Yan, Q.J. Few-layered $Ni(OH)_2$ nanosheets for high-performance supercapacitors. *Power Sources* **2015**, *295*, 323–328. [CrossRef]
33. Niu, H.; Zhou, D.; Yang, X.; Li, X.; Wang, Q.; Qu, F.J. Towards three-dimensional hierarchical ZnO nanofiber@$Ni(OH)_2$ nanoflake core–shell heterostructures for high-performance asymmetric supercapacitors. *Mater. Chem. A* **2015**, *3*, 18413–18421. [CrossRef]
34. Ji, J.; Zhang, L.L.; Ji, H.; Li, Y.; Zhao, X.; Bai, X.; Fan, X.; Zhang, F.; Ruoff, R.S. Nanoporous $Ni(OH)_2$ thin film on 3D Ultrathin-graphite foam for asymmetric supercapacitor. *ACS Nano* **2013**, *7*, 6237–6243. [CrossRef]
35. Yang, S.H.; Lee, Y.J.; Kang, H.; Park, S.K.; Kang, Y.C. Carbon-Coated Three-Dimensional MXene/Iron Selenide Ball with Core-Shell Structure for High-Performance Potassium-Ion Batteries. *Nano Micro Lett.* **2021**, *14*, 17. [CrossRef]
36. Wang, F.; Liu, X.; Chen, F.; Wan, H.; Lin, Y.; Zhang, N.; Ma, R. Advanced supercapacitors based on α-$Ni(OH)_2$ nanoplates/graphene composite electrodes with high energy and power density. *ACS Appl. Energy Mater.* **2018**, *1*, 1496–1505. [CrossRef]
37. Chai, Y.Q.; Li, Z.P.; Wang, J.Q.; Mo, Z.L.; Yang, S.R. Construction of hierarchical holey graphene/MnO_2 composites as potential electrode materials for supercapacitors. *J. Alloy. Comp.* **2019**, *775*, 1206–1212. [CrossRef]
38. Li, Y.J.; Yu, N.; Yan, P.; Li, Y.G.; Zhou, X.M.; Chen, S.L.; Wang, G.L.; Wei, T.; Fan, Z.J. Fabrication of manganese dioxide nanoplates anchoring on biomass-derived cross-linked carbon nanosheets for high-performance asymmetric supercapacitors. *J. Power Sources* **2015**, *300*, 309–317. [CrossRef]
39. Zhang, Y.N.; Mao, T.Y.; Cheng, L.F.; Wu, H.; Wu, R.; Zheng, L.N. Tunable morphology and property of a MnO_2/carbonized cotton textile hybrid electrode for electrochemical capacitors. *J. Alloy. Comp.* **2017**, *729*, 655–662. [CrossRef]
40. Atchudan, R.; Edison, T.N.J.I.; Perumal, S.; Lee, Y.R. Green synthesis of nitrogen-doped graphitic carbon sheets with use of Prunus persica for supercapacitor applications. *Appl. Surf. Sci.* **2017**, *393*, 276–286. [CrossRef]
41. Zheng, S.; Wang, H.; Das, P.; Zhang, Y.; Cao, Y.; Ma, J.; Liu, S.F.; Wu, Z.S. Multitasking MXene Inks Enable High-Performance Printable Microelectrochemical Energy Storage Devices for All-Flexible Self-Powered Integrated Systems. *Adv. Mater.* **2021**, *33*, e2005449. [CrossRef] [PubMed]
42. Zhou, Y.; Li, J.; Hu, S.; Qian, G.; Shi, J.; Zhao, S.; Wang, Y.; Wang, C.; Lian, J. Sawdust-Derived Activated Carbon with Hierarchical Pores for High-Performance Symmetric Supercapacitors. *Nanomaterials* **2022**, *12*, 810. [CrossRef] [PubMed]

43. Qiao, S.; Huang, N.; Sun, Y.; Zhang, J.; Zhang, Y.; Gao, Z.J. Microwave-assisted synthesis of novel 3D flower-like $NiMnO_3$ nanoballs as electrode material for high-performance supercapacitors. *Alloy Compd.* **2019**, *775*, 1109–1116. [CrossRef]
44. Tseng, C.A.; Sahoo, P.K.; Lee, C.P.; Lin, Y.T.; Xu, J.H.; Chen, Y.T. Synthesis of CoO-Decorated Graphene Hollow Nanoballs for High-Performance Flexible Supercapacitors. *ACS Appl. Mater. Interf.* **2020**, *12*, 40426–40432. [CrossRef] [PubMed]
45. Zhang, J.Y.; Yang, X.F.; He, Y.B.; Bai, Y.L.; Kang, L.P.; Xu, H.; Shi, F.; Lei, Z.B.; Liu, Z.H. δ-MnO_2/holey graphene hybrid fiber for all-solid-state supercapacitor. *J. Mater. Chem.* **2016**, *4*, 9088–9096. [CrossRef]
46. Ma, Z.P.; Shao, G.J.; Fan, Y.Q.; Wang, G.L.; Song, J.J.; Shen, D.J. Construction of hierarchical alpha-MnO_2 Nanowires@Ultrathin delta-MnO_2 nanosheets core-shell nanostructure with excellent cycling stability for high-power asymmetric supercapacitor electrodes. *ACS Appl. Mater. Interfaces* **2016**, *8*, 9050–9058. [CrossRef] [PubMed]
47. Wang, N.; Zhao, P.; Liang, K.; Yao, M.Q.; Yang, Y.; Hu, W.C. CVD-grown polypyrrole nanofilms on highly mesoporous structure MnO_2 for high performance asymmetric supercapacitors. *Chem. Eng. J.* **2017**, *307*, 105–112. [CrossRef]
48. Yan, X.C.; Jia, Y.; Zhuang, L.Z.; Zhang, L.Z.; Wang, K.; Yao, X.D. Defective carbons derived from macadamia nut shell biomass for efficient oxygen reduction and supercapacitors. *ChemElectroChem* **2018**, *5*, 1874–1879. [CrossRef]